Study of the Composition and Structure of High-Strength Material Based on a Fine High-Calcium Fly Ash Using the SEM-EDS Method

Olga Sharonova *, Anatoliy Zhizhaev, Vladimir Yumashev

Posted Date: 17 April 2026

doi: 10.20944/preprints202604.1189.v1

Keywords: high calcium fly ash; microspheres; SEM-EDS; compressive strength; hydration products; thermal analysis

 doi:10.20944/preprints202604.1189.v1

Article

Study of the Composition and Structure of High-Strength Material Based on a Fine High-Calcium Fly Ash Using the SEM-EDS Method

Olga Sharonova *, Anatoliy Zhizhaev and Vladimir Yumashev

Institute of Chemistry and Chemical Technology SB RAS, Federal Research Center "Krasnoyarsk Science Center SB RAS", Krasnoyarsk 660036, Russian Federation

* Correspondence: shar@icct.ru or sharon05@yandex.ru

Abstract

This study examines the microspherical high-calcium fly ash (HCFA) and the high-strength binder material based on it by method of scanning electron microscopy and energy-dispersive X-ray spectroscopy (SEM-EDS). The composition of 568 individual microspheres of the initial HCFA was determined and presented as ternary diagrams $CaO–Al_2O_3–SiO_2$ and $CaO–FeO–SiO_2$. The binder specimens have a compressive strength of 24–90 MPa at a curing time of 3–300 days. Their strength is close to that of CEM I 42.5N cement specimens with a curing time of up to 28 days, but exceeds it with a curing time of up to 300 days. The SEM-EDS method showed that the predominant composition of hydration products is concentrated in the high-calcium region of the $CaO–Al_2O_3–SiO_2$ diagram with a CaO content of 60–80%. The SiO_2 content in them is 15-30%, and their composition includes 1–15% Al_2O_3 and 5–14% FeO. The SEM-EDS method allowed us to understand the transformation of calcium silicate glass microspheres into C-S-H gel, which is the main component of the strengthening matrix. The results contribute to the data for development of models for predicting the effect of HCFA on the properties of composite binders.

Keywords: high calcium fly ash; microspheres; SEM-EDS; compressive strength; hydration products; thermal analysis

1. Introduction

Large-scale solid waste from coal-fired thermal power plants (fly ash, fuel slag) is increasingly considered as a secondary raw material in various industries, which contributes to solving environmental problems and improving the competitiveness of products [1]. A particularly successful area of practical application is the use of fly ash in the construction industry as an active pozzolanic additive in the production of cement and concrete, which is a global trend [2–4]. It is well known that fine-grained coal fly ash is used in amounts ranging from 6 to 35% for various types of composite cements [5–8].The largest proportion of fly ash used is aluminosilicate fly ash of class F according to [6] or type V according to [7] due to its less variable and more uniform composition. However, due to its low reactivity, the clinker substitution limit is approximately 35% by weight [9]. More active high-calcium fly ash – class C according to [6] or type W according to [7] – can significantly increase the cement substitution limit, but there are limitations due to its significantly greater heterogeneity.

To study the influence of fly ash on the properties of blended cements, a detailed characterization of the original fly ash is necessary. The particle size of ash has a strong influence on its binding properties, so researchers often provide data on the particle size distribution [2,10,11]. Chemical composition is also an important factor; the most common method for determining the chemical composition of fly ash is X-ray fluorescence analysis (XRF) [12]. Chemical analysis methods are a more accurate and reliable method for determining the composition of fly ash [13], but it is more

 doi:10.20944/preprints202604.1189.v1

labor-intensive and therefore used much less frequently. X-ray diffraction (XRD) analysis and refinement using the Rietveld method allows quantitative determination of crystalline phases and glass content [9,12,13]. Existing characterization methods often fail to identify the composition of glass, which can constitute up to 90% of the total fly ash mass and contain a mixture of different glass compositions [9,14,15]. The composition of the glassy phase can be calculated using a combination of chemical and quantitative phase analysis data, as shown, for example, in [12] for two low-calcium fly ashes. Glass composition can also be calculated using data from these methods, as cited in [15–17]. The influence of particle size, crystalline phase composition, and glass phase of the original fly ashes is of great interest for predicting the properties of composite binders; however, this data is currently insufficient to create reliable models.

For various reasons, studies of the influence of fly ash on the properties of binders using the SEM-EDS method are becoming increasingly important. For example, in [16], the hydration products of mixed cement containing 30% aluminosilicate fly ash were investigated. After curing for 1 year, two types of regions were analyzed: the "inner products" (IP) and "outer products" (OP). "Inner products" form within the boundaries of the original particles, while "outer products" form in the space initially filled with water when it mixes with the cement particles. Calcium hydroxide $Ca(OH)_2$ forms in the same space as the external product C-S-H. Based on EDS analysis of ternary composition diagrams, it was found that the composition of the products in the Ca-Si-Al diagram differs significantly from that of hydrated pure cement in that they contain less Ca and more Si and Al. But the effect of fly ash on the strength of the material has not been investigated. The authors [17] found an increase in compressive strength by 23% with the addition of 8% finely dispersed fly ash of aluminosilicate composition (class F) with d_{mean} = 3.4 um and a high-silica glass content of 81%. Using SEM and XRD, it was established that the effect of the fly ash consists in obtaining a denser structure with a smaller number of pores, as well as in greater consumption of $Ca(OH)_2$ with the formation of additional C-S-H due to the activation of the pozzolanic reaction.

The use of silica-rich supplementary cementitious materials (SCMs) affects the amount and type of hydrates formed, and hence the volume, porosity, and ultimately the strength of these materials [18]. At commonly used substitution levels, the main changes are a lower Ca/Si ratio in the C–S–H phase and a higher consumption of $Ca(OH)_2$ in the reaction mixture. Alumina-rich SCMs increase the incorporation of Al into the C–S–H structure and the amount of calcium aluminate hydrates.

In [12], the mixtures of PC with 50% of each of two low-calcium fly ashes were studied over 550 days of hydration. No signs of a fly ash reaction were detected up to 2 days, and the effect on hydration was associated with the "filler effect." Their strength on the 28th day was half that of cement, but began to gradually increase at later stages of hardening, and the influence of a pozzolanic reaction was observed, manifested in an increase in the consumption of portlandite $Ca(OH)_2$ and a change in the chemical composition of the pore solution. Using the SEM-EDS method, the influence of fly ash on the change in the composition of the formed C–S–H was established towards a decrease in the Ca/Si ratio from 1.7 to 1.4–1.6 and an increase in the Al/Si ratio from 0.07 to 0.15–0.16 compared to the C–S–H of pure cement during hardening for 28–90 days. In addition, it was concluded that the hydration reactions with increasing strength of cement-ash samples proceed somewhat faster with fly ash, which has a lower glass content, but it has a higher Ca and Mg content. Indeed, calcium-rich glasses are generally more reactive than glasses with moderate and low calcium content [19]. Calcium acts as a modifier in the glass structure: by breaking Si–O bonds, it creates a less connected network, which, therefore, is more easily destroyed upon contact with aqueous solutions.

High-calcium ash is more difficult to characterize due to the greater variability of the crystalline phases and the heterogeneity of the glasses. This is mainly due to the lack of appropriate methods for both the characterization of raw ash and the measurement of its reaction in hydrated mixed cement [9]. Wavelength-dispersive electron microscopy (WDS) or energy-dispersive X-ray spectroscopy (EDS) are the most common methods for studying glass in ash and analyzing the chemical composition of different particles [20–22]. In this regard, the authors [9] developed an approach for SEM-EDS characterization of ash using a new generation of fast EDS detectors, with spectral

 doi:10.20944/preprints202604.1189.v1

processing and data analysis using MultiSpec©, a multispectral image analysis software that uses a clustering algorithm to identify and quantify groups of mutually exclusive chemical compositions. The elemental composition of millions of points, determined by EDS method, is presented on a three-component frequency diagram. Visual analysis reveals the number and ranges of chemical composition of four populations: (1) silicate, (2) calcium-silicate, (3) aluminosilicate, and (4) calcium-rich aluminosilicate. The authors quantified these populations in four ash-bearing units and monitored their hydration in mixtures of Portland cement PC 55% - ash-bearing unit 45% for two ash-bearing units. It has been established that calcium-rich aluminosilicates are the most reactive and, accounting for more than 50% of the FA2 ash, make the greatest contribution to the overall hydration transformation reaction. However, data on the direct effect on strength are not presented in [9].

There is growing interest in individual fly ash particles, classifying them by composition and determining their reactivity in hydration transformation. On this basis, a new approach to predicting the strength of concrete containing fly ash, called the Particle Model [23,24], is being developed, which uses ASEM-EDS (automated scanning electron microscopy with energy dispersive X-ray spectrometry). Thousands of fly ash particles are classified into nine groups based on the chemical composition of each particle. Predictive compressive strength models are developed for fly ash substitution levels of 20% and 40% for seven different curing times ranging from 3 to 180 days. The R-squared value for predicting compressive strength in the particle model is ≈ 0.99, while for models for fly ash classes C and F it is <0.50.

In this work, the aim was to study the composition of individual microspheres of the original finely dispersed high-calcium fly ash, to obtain a hardened binder material based on this fly ash at different curing times and to study the composition and structure of this material using the SEM-EDX method.

2. Results and Discussion

2.1. Individual Microspheres of the Original HCFA

The original HCFA is a finely dispersed microspherical material; the microsphere size distribution is shown in Figure 1a. It was determined that 90% of the microspheres in this FA (curve FA) have a size of less than 10 μm (d90-10 μm), and 50% are less than 4 μm (d50-4 μm). The particle size distribution for cement (curve PC), compared to FA, is shifted towards larger particles: d90 and d50 are 55 and 20 μm, respectively.

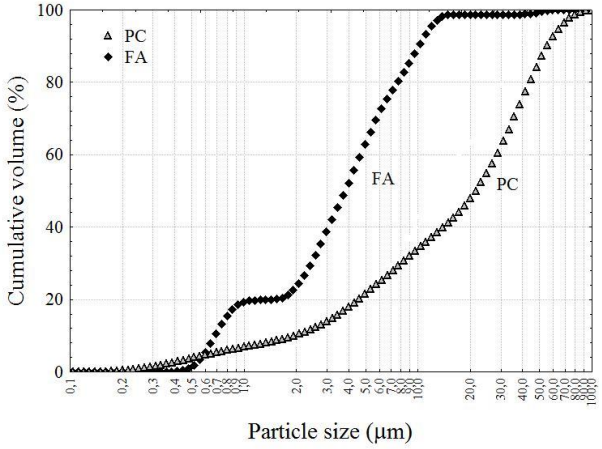

a

 doi:10.20944/preprints202604.1189.v1

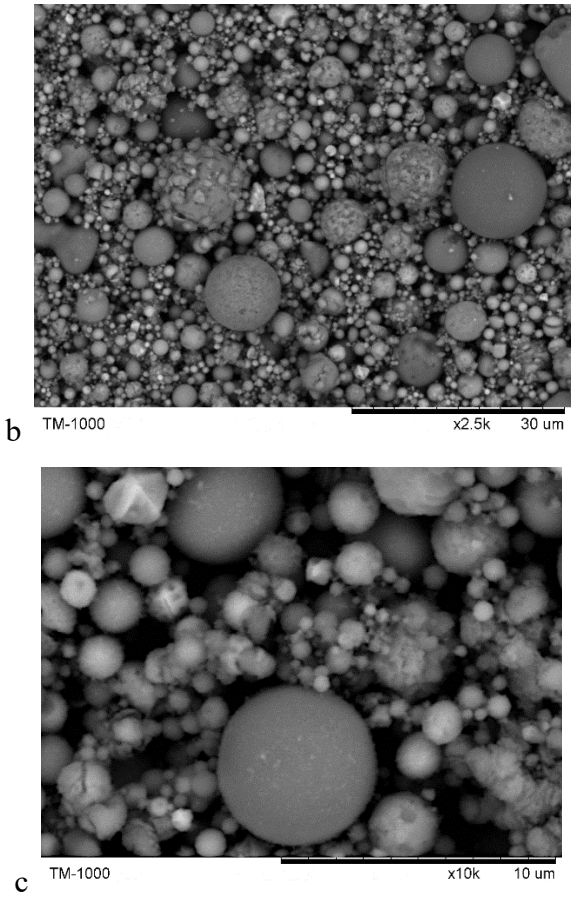

Figure 1. Particle size distribution (a) for the original fly ash (FA) and cement (PC) and SEM images (b and c) of the original HCFA.

In the chemical composition of the original HCFA, the content of the main components is (wt.%) [25,26]: CaO 39.7; SiO_2 24.6; Al_2O_3 7.3; Fe_2O_3 14.3; MgO 8.2; SO_3 2.3; Na_2O 0.7; K_2O 0.2; TiO_2 0.3. It follows that the dominant component is CaO (39.7 wt.%), with SiO2 present to a lesser extent (24.6 wt.%). This HCFA differs from the composition of PC 42.5N cement [27] by a lower CaO content (by 1.6 times), but a higher content of SiO_2, Al_2O_3, Fe_2O_3 and MgO components.

According to SEM data (Figure 1b and c), this HCFA consists of microspheres of varying morphology. Microspherical globules with a relatively smooth surface have an aluminosilicate composition with variable Al/Si ratios (Figure 2a and 2 b) or a calcium-silicate composition with a significant contribution of Al and Fe (Figure 2c). Globules with a textured surface (Figure 2d, e, f) are dominated by calcium, have highly variable Ca/Si ratios, and variable contributions of macrocomponents such as Al, Fe, Mg, and S.

 doi:10.20944/preprints202604.1189.v1

a

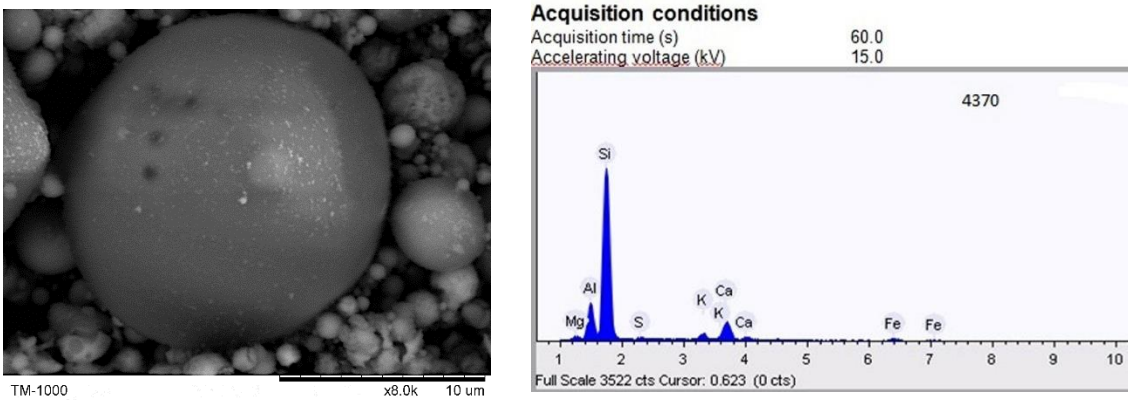

b

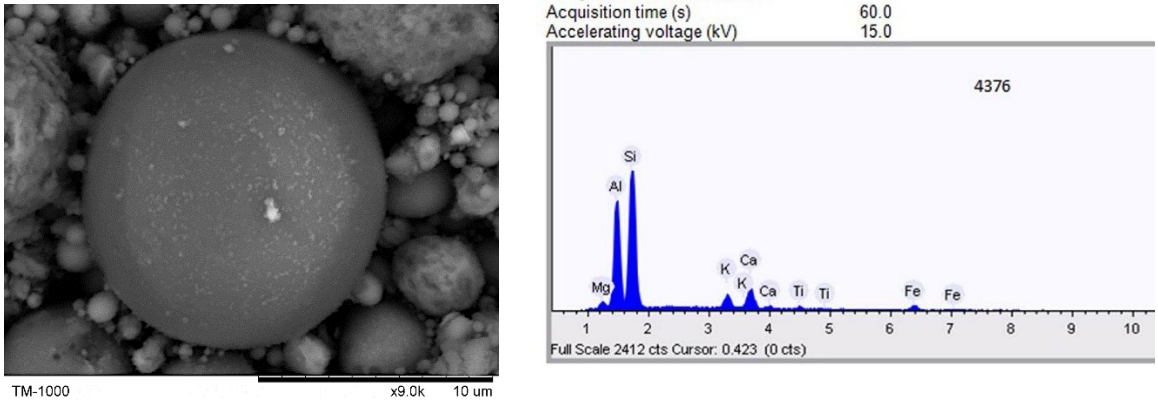

c

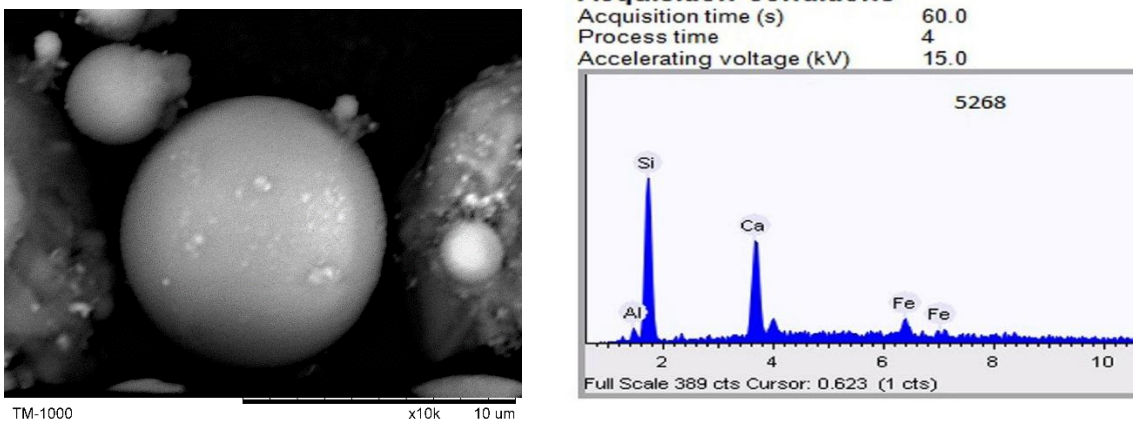

d

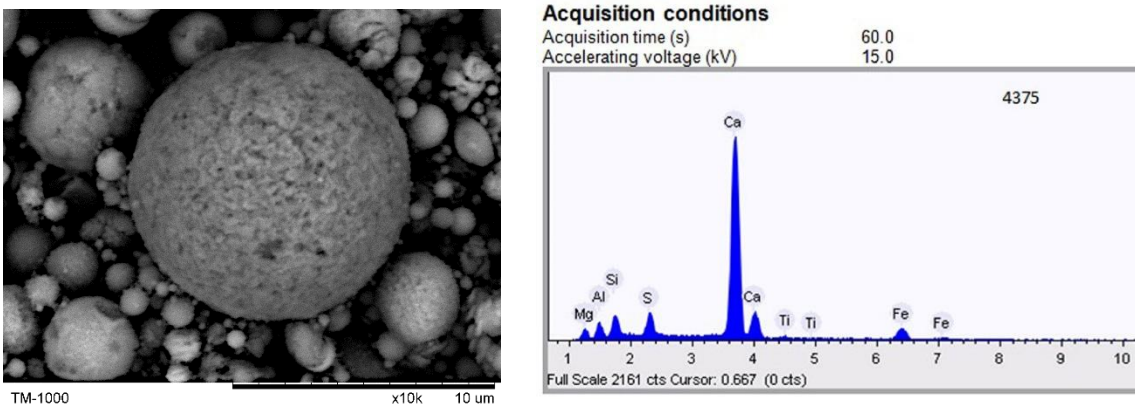

 doi:10.20944/preprints202604.1189.v1

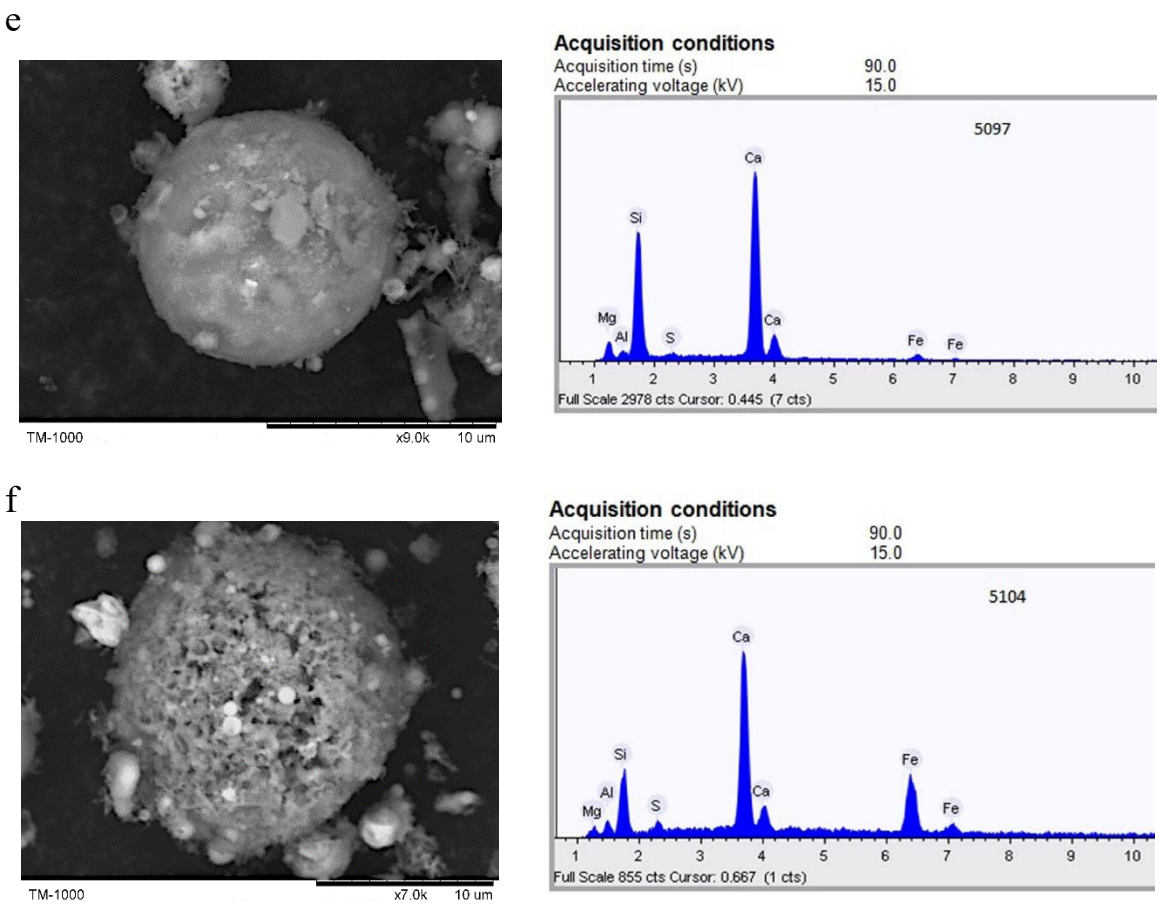

Figure 2. SEM images and EDS spectra of individual microspheres of different compositions:.a, b, c – globules with a smooth surface; d, e, f – globules with a relief surface.

The SEM-EDX analysis of the composition of individual microspheres was performed for 568 globules, the size distribution of which is shown in Figure. 3. It is evident that the main contribution is made by microspheres with a diameter of 1< d < 2 μm (45%) and 2< d <4 μm (37%).

The chemical composition of individual globules, presented in the form of ternary diagrams of the composition $CaO-Al_2O_3-SiO_2$ (Figure 4 a) and $CaO-FeO-SiO_2$ (Figure 4b), indicates its wide scatter. However, it should be noted that the overwhelming majority of compositions are in the range with a CaO content of 50-90%, where the content of SiO_2 and Al_2O_3 in Figure 4a or SiO_2 and FeO in Figure 4b is 2-25% each.

 doi:10.20944/preprints202604.1189.v1

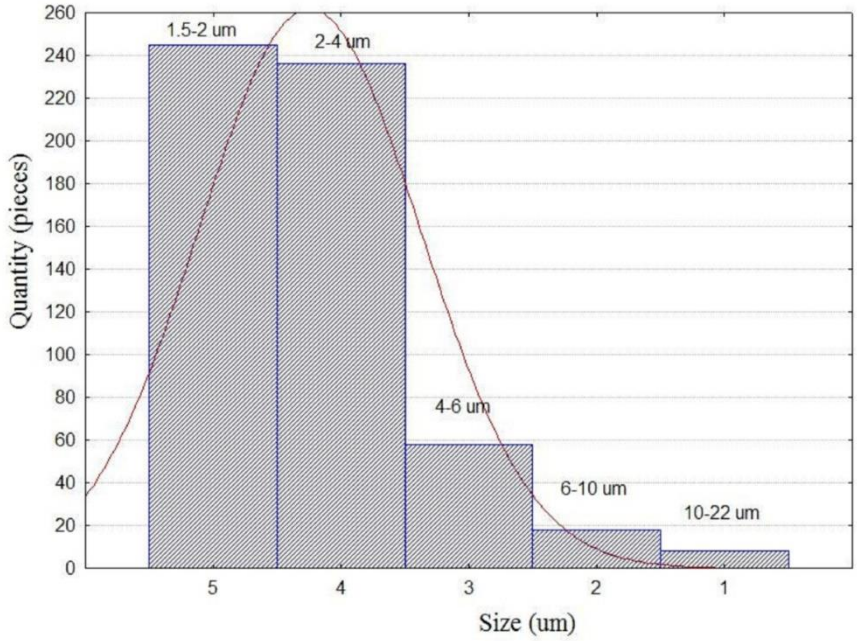

Figure 3. Contribution of individual microspheres of different sizes according to SEM data.

Microspheres with a CaO content of 5-50% exhibit distinct compositional trends. The CaO-Al2O3-SiO2 diagram (Figure 4a) shows trend 1 for calcium-silicate microspheres with a CaO/SiO2 ratio ranging from 0.05 to 2.3, and trend 2 for calcium-aluminosilicate microspheres. The CaO-FeO-SiO2 diagram (Figure 4b) also shows trend 1, and trend 3 for the calcium-iron-silicate composition, transitioning to the calcium-ferrite compositions of the globules.

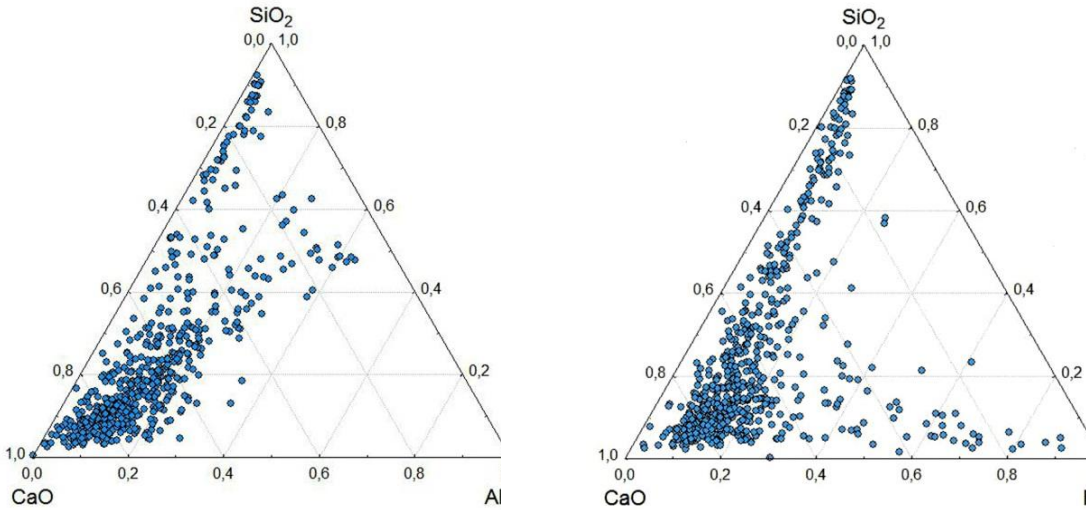

a **b**

Figure 4. Composition of 568 individual microspheres of the original HCFA in ternary diagrams of the composition CaO-Al_2O_3-SiO_2 (a) and CaO-FeO-SiO_2 (b).

2.2. Specimens of Binders at Different Curing Times

Figure 5 shows the compressive strength of cured binders based on finely dispersed HCFA (curve 1) and CEM I 42.5N cement (curve 2) with curing periods ranging from 3 to 300 days. When cured for up to 28 days, their strengths are virtually identical, remaining at approximately 50 MPa. For the PC sample, after 80 days, the strength increases to 60-66 MPa and remains within this range until 300 days. Similar behavior for this grade of cement was observed by the authors [28], where the

 doi:10.20944/preprints202604.1189.v1

compressive strength was approximately 54 MPa after 28 days, increased to 70 MPa after 80 days, and remained at this level until 350 days of curing. For the binder based on fine HCFA (curve 1), higher strength was observed after 50 days compared to cement specimens (curve 2) and amounted to 80-90 MPa after 300 days of hardening. A similar increase in strength to 90 MPa at 300 days was observed by the authors [28] for composite cement containing 25% ultrafine aluminosilicate cementitious material, ground in a planetary mill to a size of less than 7 μm, in the presence of a polycarboxylate superplasticizer. The authors [28] attribute this effect to a more compact structure, and to a lesser extent to the additional pozzolanic reaction of the cementitious material with $Ca(OH)_2$. However, the increase in the strength of the binder based on fine HCFA should be associated with hydration transformations of crystalline phases and glass into additional hydrate products.

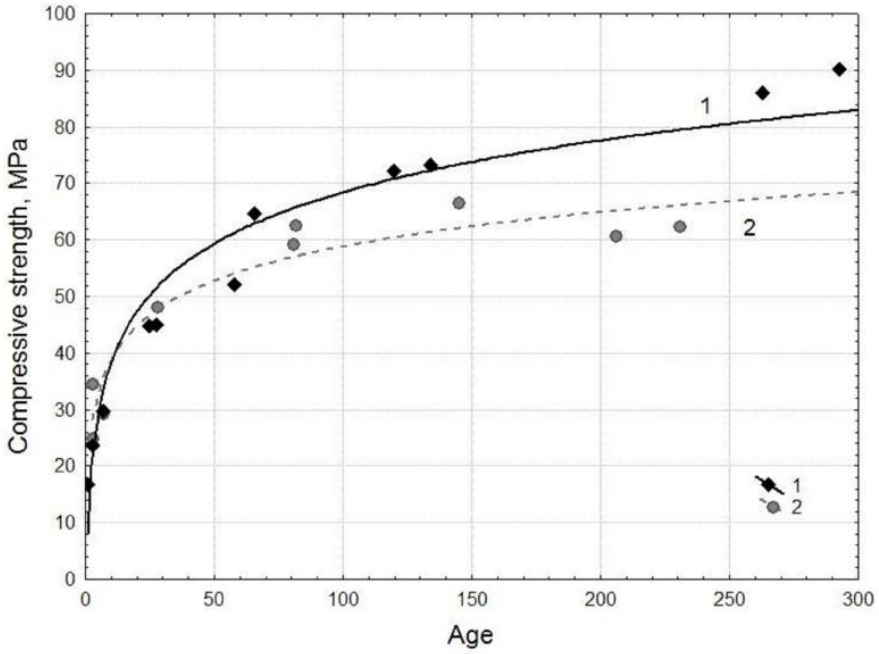

Figure 5. Compressive strength of binder based on fine HCFA (1) and cement CEM I 42.5N (2) with curing time of up to 300 days.

SEM images of the binder after 3 and 60 days of hydration curing are shown in Figure 6. These images show that, as early as the third day, the space around the microspheres is filled with newly formed phases, forming a strength matrix that provides a compressive strength of approximately 24 MPa. However, a large proportion of the microspheres remain virtually unreacted. As the curing time increases to 60 days, the filling density increases, the strength increases to 58±6 MPa, and the number of "unreacted" microspheres decreases.

 doi:10.20944/preprints202604.1189.v1

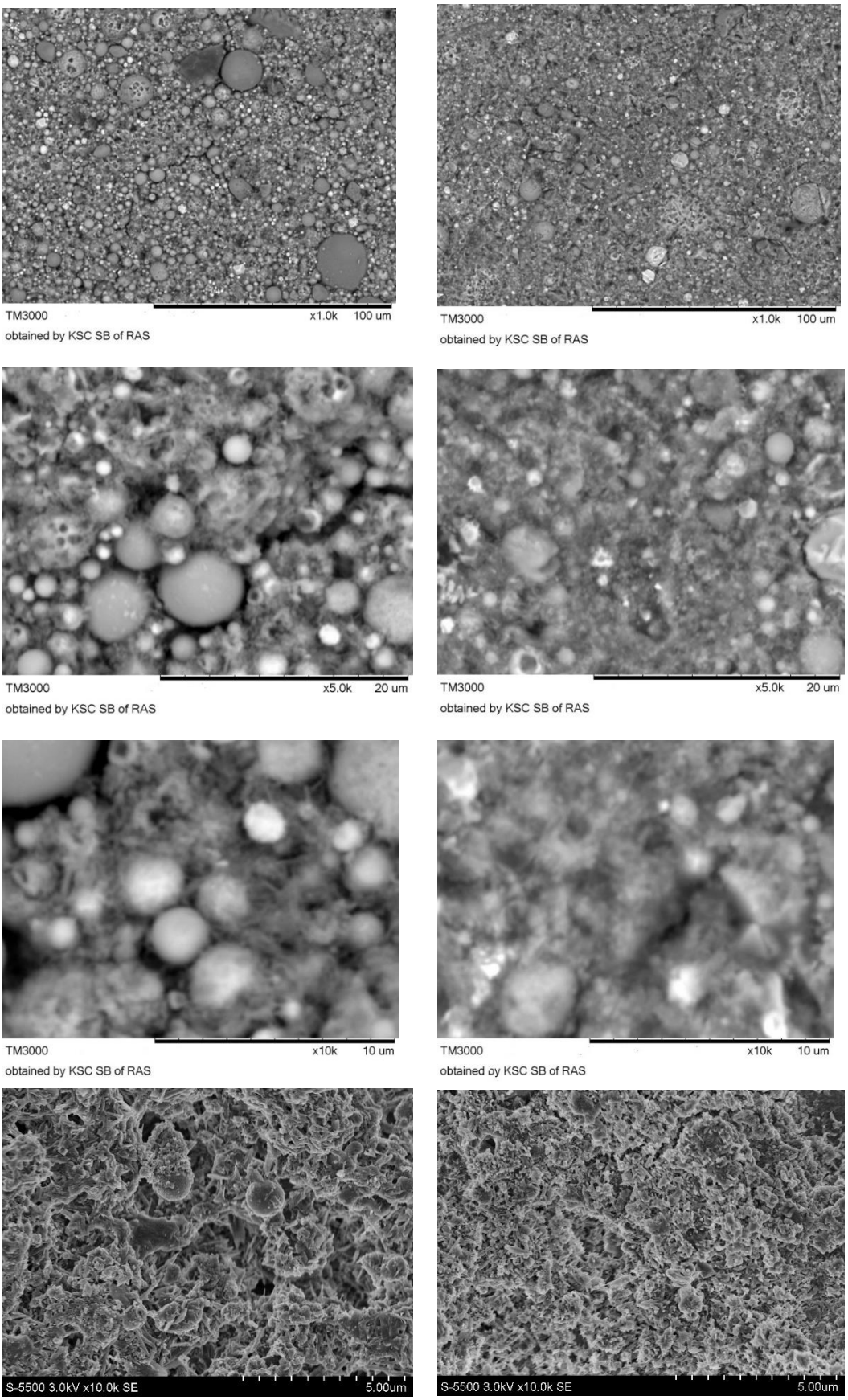

a **b**

Figure 6. SEM images of cured material based on a fine HCFA : a – after 3 days and b – after 60 days of age.

 doi:10.20944/preprints202604.1189.v1

To analyze the composition of hardened material sections, researchers use the terms "outer products" (OP) and "inner products" (IP), or the terms "bulk mass" and "phenogens," meaning "separate" [16]. The "outer products" and "bulk mass" include new formations in the form of hydrate products in the space initially filled with water, which form the strength matrix. In contrast, the "inner products" are unreacted or, to varying degrees, modified by interaction with the environment, original microspheres.

Figure 7a shows the compositions of OP sections on days 3 and 60 of hardening in the CaO–Al_2O_3–SiO_2 ternary diagram. It is evident that the overwhelming majority of the OP compositions are concentrated in the high-calcium region of the diagram with a total CaO content of 60-80%. The SiO_2 content here is about 15-30%. In addition, according to EDS data, their composition may include from 1 to 15% Al_2O_3, 5-14% FeO and 1-10% MgO. The CaO/SiO_2 ratio varies from 1.7 to 4.2, which is very close to the composition of the hardened cement sections in the CaO–Al_2O_3–SiO_2 composition diagram according to [12,16]. From the totality of these data it follows that the main products of hydration hardening are calcium hydrosilicates. It also follows from Figure 7a that the aluminum content in the hydration products after 3 days is lower compared to the products after 60 days.

The CaO–FeO–SiO_2 diagram (Figure 7b) shows that the iron content of the hydration products is somewhat higher than the aluminum content, and it is independent of curing time. One of the reasons for this effect is the more active role of calcium aluminoferrite $Ca_2Fe_xAl_yO_5$ compared to calcium aluminate $Ca_3Al_2O_6$ in the formation of ettringite $3CaO \bullet (Al, Fe)_2O_3 \bullet 3CaSO_4 \bullet 32H_2O$ when interacting with $CaSO4 \bullet 2H_2O$.

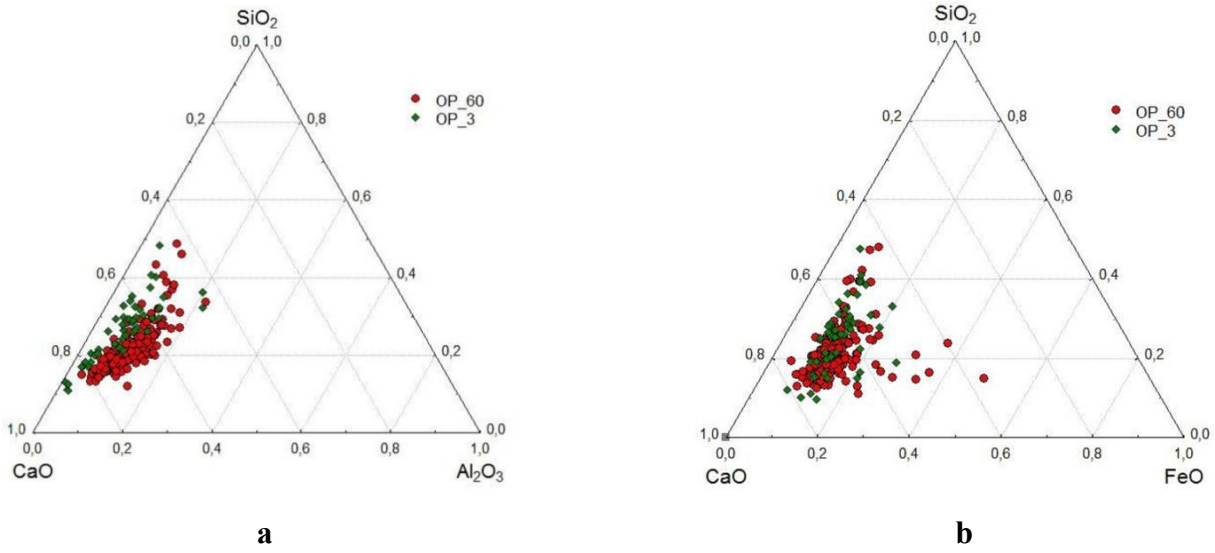

Figure 7. The composition of the "outer products" (OP) areas in binder specimens after 3 and 60 days of hardening on the CaO-Al_2O_3-SiO_2 (a) and CaO-FeO-SiO_2 (b) ternary diagrams.

It was previously established [25,27] that in this finely dispersed HCFA, calcium aluminoferrite reacts more actively than calcium aluminate, and that the interaction of $Ca_2Fe_xAl_yO_5$ with $CaSO_4$ can form an almost continuous series of solid solutions of Al,Fe-ettringites. The results obtained by the SEM-EDS method in this work are consistent with the data obtained in [25,27] and confirm the more active role of calcium aluminoferrites. This is the difference between the studied HCFA and Portland cement, in the latter, calcium aluminate underwent a more active transformation, forming ettringite $3CaO \bullet Al_2O_3 \bullet 3CaSO4 \bullet 32H_2O$ [25] during hydration hardening of PC.

One of the main contributions to the hydrate transformations of cement and HCFA is the dissolution of CaO with its transition into the pore solution in the form of $Ca(OH)_2$, which is consistent with the data of thermal analysis (Figure 8).

 doi:10.20944/preprints202604.1189.v1

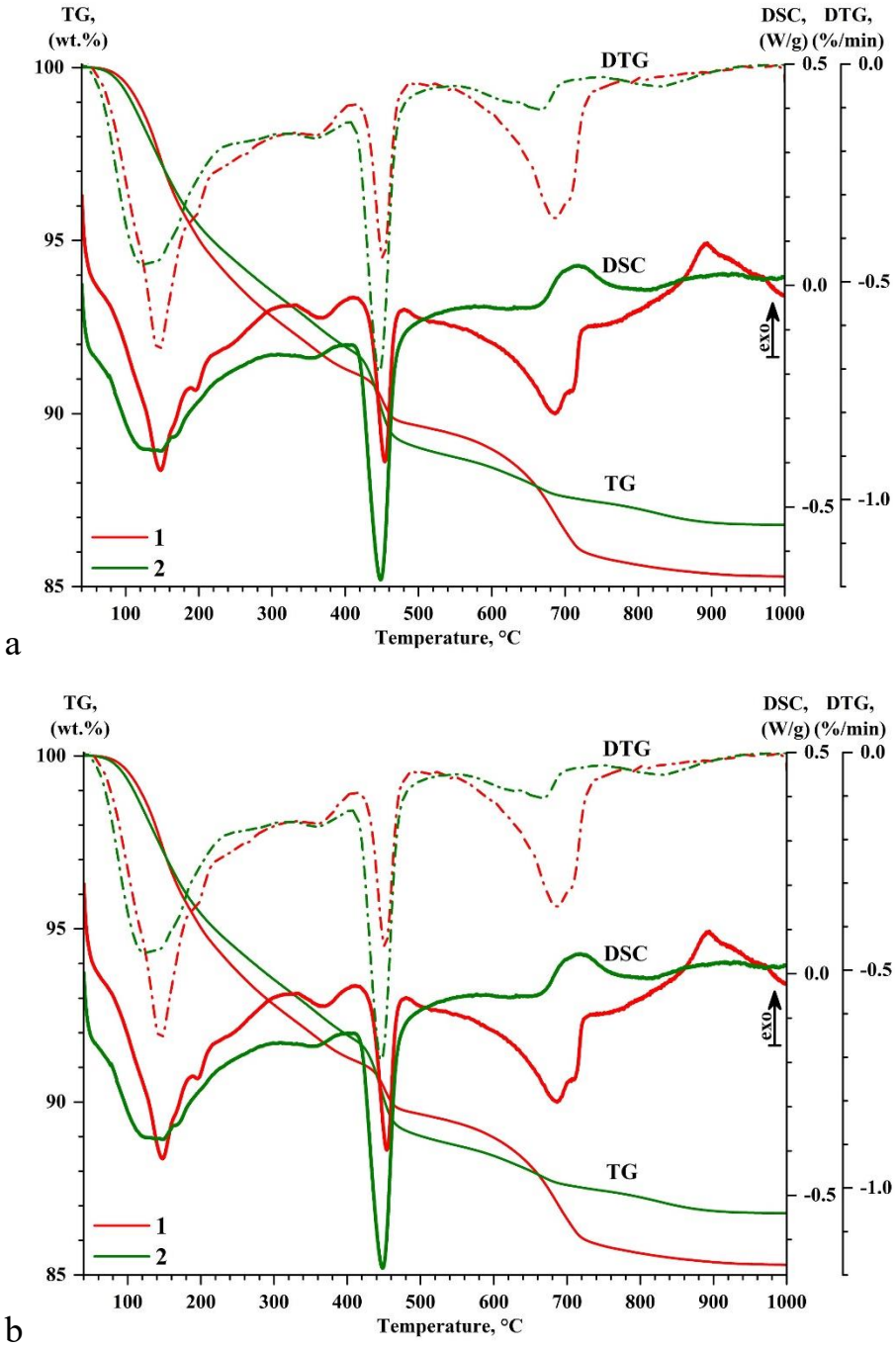

Figure 8. STA data for cement CEM I 42.5N binder (a) and TG, DTG and DSC data for binders (b) based HCFA (1) and PC (2) on the 28th day of hardening.

Figure 8a shows the data for a specimen based on 100% CEM I 42.5N cement after 28 days of hardening, from which it follows that the mass loss in the form of H_2O from the dehydration of Ca(OH)2 in the temperature range of 410-520°C with an extremum at 448°C is 2.9%, which corresponds to a content of about 12% $Ca(OH)_2$ and is consistent with the data of XDR analysis (the content of $Ca(OH)_2$ is 11.7% under similar hardening conditions [27]. From the comparison of the TG-DTG-DSC data in Figure 8b for HCFA (curves 1) and cement (curves 2), some differences are observed, consisting in a smaller mass loss from the dehydration of $Ca(OH)_2$ in the temperature range of 410-520 °C with an extremum at 454 °C and the nature of the dehydration of the products in the temperature range of 40-320 °C. In particular, a more pronounced endothermic effect is observed in the DSC curves with an extremum at 148 °C and inflections at 195 and 244 °C.

 doi:10.20944/preprints202604.1189.v1

In the literature, endothermic peaks in the dehydration range below 320 °C are associated with the removal of the main part of the water from ettringite, as well as from weakly crystallized and amorphous phases of calcium hydrosilicates [11,12,26]. In the range of 200-320°C, the amount of which also continuously increases and which is associated with the dehydration of the AFm phases and more ordered structures of calcium hydrosilicates [12]. In addition, significant mass losses are observed due to the decarbonization of $CaCO_3$ in the range of 520-750°C with an extremum at 687°C as a consequence, among other things, of the decomposition of carboaluminates [26].

Analysis of the "inner products" sections of the $CaO–Al_2O_3–SiO_2$ diagram (Figure 9a) reveals three trends: (1) sections of calcium silicates with a SiO_2 content greater than 50%, which increases from 50 to 80% with a decrease in CaO from 50 to 20%; (2) sections of calcium-aluminosilicate composition, in which the CaO/Al_2O_3 ratio mainly changes with a relatively constant SiO_2 content in the range of 40–50%, and (3) sections of predominantly calcium-aluminate composition with a SiO_2 content of 6–15%. The data from the analysis of the products of section (3) lie along the line connecting the cluster of internal products with the AFm and $Ca_3Al_2O_6$ compositions.

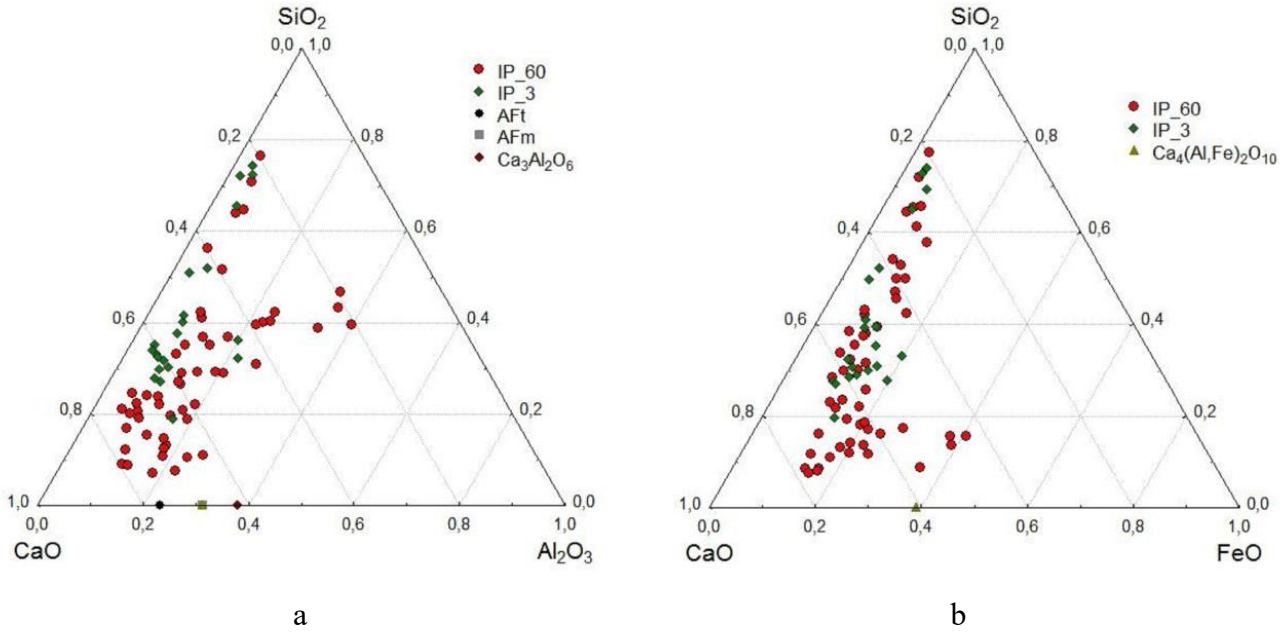

Figure 9. The composition of the "inner products" (IP) areas in binder specimens after 3 and 60 days of hardening on the $CaO-Al_2O_3-SiO_2$ (a) and $CaO-FeO-SiO_2$ (b) ternary diagrams.

The formation of AFm phases is described in [25], where, under conditions of sulfate ion deficiency for binding $Ca_2Fe_xAl_yO_5$ into ettringite, the $Ca_2Fe_xAlyO_5$ phase actively participates in the formation of calcium carboaluminate hydrates, which belong to the so-called AFm phases. It is known that calcium aluminoferrite hydrates in the presence of $Ca(OH)_2$ and $CaSO_4$ can form AFm phases of the general composition $[Ca_2(Al,Fe)(OH)_6]•X•xH_2O$, where X is one singly charged anion or 0.5 of a divalent anion. X can be OH-, SO_4^{2-}, and CO_3^{2-} anions. It is worth noting that the Al- and Fe-substituted AFm phases are isostructural analogues and, depending on the temperature, form solid solutions of different miscibility.

The $CaO–FeO–SiO_2$ diagram (Figure 9b) shows, in addition to the calcium-silicate trend, a trend toward a predominantly calcium-iron-silicate composition. The compositions of the IP sections with a CaO content of 50–80% in this diagram are shifted toward higher iron content (10–20%) compared to Figure 4b, possibly related to the reduced solubility of calcium-iron-silicate glass in the surrounding alkaline solution.

 doi:10.20944/preprints202604.1189.v1

3. Conclusions

1. SEM-EDS was used to study 568 individual microspheres in the original fine high-calcium fly ash with a particle size of d90–10 μm. Analysis of the composition of individual globules using ternary diagrams of CaO-Al_2O_3-SiO_2 and CaO-FeO-SiO_2 reveals a wide range of compositions. However, most microsphere compositions are in the array with a content of CaO 55–90%, SiO_2 5–30%, Al_2O_3 0–20% and FeO 2–25%. When the CaO content is less than 50%, there are three trends in the composition of microspheres: (1) calcium silicates, (2) calcium aluminosilicates, and (3) calcium-iron-silicates and calcium ferrites.
2. Based on fine HCFA, the specimens were obtained (at W/B=0.25; superplasticizer 0.12% Melflux 5581F) with high compressive strength, which increases from 24 to 90 MPa during curing from 3 to 300 days. Comparison with specimens based on CEM I 42.5N cement (at W/C=0.4) showed that during curing up to 28 days their strength is practically the same and amounts to about 50 MPa. With further curing up to 300 days, the strength of the cement samples (60-66 MPa) is inferior to the specimens based on HCFA.
3. Using the SEM-EDS method, the compositions of 410 areas of newly formed hydrate products in a space initially filled with water, which forms the strength matrix, were studied. It was found that the overwhelming majority of the compositions are concentrated in the high-calcium region of the CaO–Al_2O_3–SiO_2 diagram, with a total CaO content of 60-80%. The SiO_2 content in them is 15-30%, and they can contain from 1 to 15% Al_2O_3 and 5-14% FeO. In terms of composition and CaO/SiO_2 ratio (from 1.7 to 4.2), they are close to the composition of the areas of hardened cement in the corresponding composition diagram. The SEM-EDS method confirmed a more active role of calcium aluminoferrite in the formation of hydrate products compared to calcium aluminate.

4. Materials and Methods

4.1. Starting Materials and Binder Specimens.

The study utilized high-calcium fly ash obtained from the pulverized combustion of grade B2 brown coal from the Kansk-Achinsk Basin in BKZ-420 boiler units with liquid slag removal at a temperature of 1400-1500°C. The fly ash was collected from the 4th field of electrostatic precipitators at Krasnoyarsk Thermal Power Plant-2. Portland cement CEM I 42.5N (PC) from the Krasnoyarsk Cement Plant was used as reference samples.

Cured specimens in the form of 20x20x20 mm cubes were prepared from 100% HCFA with a W/B ratio of 0.25 and the addition of 0.12 wt.% of the high-ranking superplasticizer Melflux 5581F. Comparison samples were prepared from 100% PC with a W/C ratio of 0.4. The samples were stored in a desiccator above a layer of water for 1-300 days.

4.2. Methods

The methods for determining the particle size, chemical, and phase composition of the studied HCFA have been described in detail previously [25]. The particle size distribution (Figure 1a) was obtained using an Analysette 22 MicroTec laser particle analyzer (Fritsch, Germany) with a dry cell. The macrocomponent composition (SiO_2, Al_2O_3, Fe_2O_3, CaO, MgO, SO_3, Na_2O, K_2O, TiO_2) and loss on ignition were determined using chemical analysis methods according to GOST 5382-2019 [26]. The quantitative phase composition was calculated using the full-profile Rietveld method and derivative difference minimization. X-ray diffraction patterns were recorded in reflection geometry using CoKα radiation using an X'Pert PRO diffractometer (PANalytical, the Netherlands) with a PIXcel detector and a graphite monochromator.

To study the morphology of the samples, TM-1000 and TM-3000 scanning electron microscopes (Hitachi, Japan) were used. The composition of individual microspheres (1.5–22 μm in size) was studied using scanning electron microscopy with an energy-dispersive X-ray spectrometer (SEM-EDS) on a TM-3000 scanning electron microscope (Hitachi, Japan) equipped with a Quantax 70

 doi:10.20944/preprints202604.1189.v1

microanalysis system with a Bruker XFlash 430H energy-dispersive X-ray spectrometer at a magnification of 4000× and an accelerating voltage of 15 kV. The data acquisition time was determined by the quality of the spectrum assembly and was at least 10 minutes. For each analyzed globule (568 pieces), the general composition was determined, including the content of the elements O, Si, Al, Fe, Ca, Mg, Na, K, Ti and S. The elemental composition was converted into oxides, the iron content into FeO, and normalized to 100%.

To study the composition of the cured samples in detail, polished sections were prepared using materials and equipment from STRUERS (Denmark) and a platinum layer approximately 20 nm thick was deposited. The composition of the polished sections (410 areas) was examined using a TM-3000 scanning electron microscope (Hitachi, Japan) equipped with a Bruker microanalysis system, including an energy-dispersive X-ray spectrometer with an XFlash 430 H detector and QUANTAX 70 software (Bruker, Germany), at a resolution of 30 nm, an accelerating voltage of 15 kV, an accumulation time of more than 10 min, and the mapping mode. The elemental content was recalculated as oxides, and the sum of the oxide concentrations was normalized to 100%.

Synchronous thermal analysis (STA) of hydrated samples after drying for 2 hours at 60 °C was performed on a Jupiter STA 449C instrument (Netzsch, Germany) with an Aeolos QMS 403C mass spectral analyzer (Netzsch, Germany) in Pt-Rh crucibles with a lid using a sample weight of 20.0 ± 0.1 mg. Registration of changes in mass (TG, DTG), heat flow (DSC) and composition of gaseous products (for molecular ions Ar+, O2+, CO^{2+}, CO^{+}, H_2O^{+} and SO_2^{+}) were carried out in the mode of a linear temperature increase at a rate of 10 °C/min in the temperature range of 40-1000 °C with the supply of a gas mixture of 20% O_2 + 80% Ar (total flow - 50 cm3NTD/min). The sensitivity coefficient of the DSC-TG sensor was determined from the heat capacity of a standard sapphire disk; the relative error in determining ΔH did not exceed 4%.

The strength tests of the samples were performed using a bench-top two-column testing machine Instron model 3360 (Instron, USA) with a crosshead speed of 5 mm/min.

Author Contributions: Conceptualization, O.S., A.Z.; methodology, O.S., A.Z., and V.Yu.; validation, O.S., A.Z., and V.Yu.; investigation, O.S., A.Z., and V.Yu.; resources, O.S., A.Z., and V.Yu.; data curation, O.S., A.Z., and V.Yu.; writing—original draft preparation, O.S; writing—review and editing, O.S., A.Z., and V.Yu.; visualization, O.S., A.Z., and V.Yu.. All authors have read and agreed to the published version of the manuscript.

Acknowledgments: The work was carried out within the framework of the state assignment of the Institute of Chemistry and Chemical Technology of the Siberian Branch of the Russian Academy of Sciences, a separate division of the Federal Research Center of the Krasnoyarsk Scientific Center of the Siberian Branch of the Russian Academy of Sciences (project FWES-2026–0011) using the equipment of the Krasnoyarsk Regional Center for Collective Use of the Federal Research Center of the Krasnoyarsk Scientific Center of the Siberian Branch of the Russian Academy of Sciences.

Conflicts of Interest: The authors declare no conflicts of interest.

Abbreviations

The following abbreviations are used in this manuscript:

HCFA	High-calcium fly ash
SEM-EDS	Scanning electron microscopy and Energy-dispersive X-ray spectroscopy
XRF	X-ray fluorescence analysis
XRD	X-ray diffraction
OP	Outer products
IP	Inner products
SPMs	Supplementary cementitious materials
WDS	Wavelength-dispersive electron microscopy
ASEM-EDS	Automated scanning electron microscopy with Energy dispersive X-ray spectrometry
STA	Synchronous thermal analysis

 doi:10.20944/preprints202604.1189.v1

TG	Thermogravimetry
DTG	Derivative Thermogravimetry
DSC	Differential Scanning Calorimetry
W/B	Water/Binder
W/C	Water/Cement

References

1. Gollakota, A.R.K.; Volli, V.; ShuCh-M. Progressive utilisation prospects of coal fly ash: A review. *Sci Total Environ.* **2019**, *672*, 951–989. https://doi.org/10.1016/j.scitotenv.2019.03.337 .
2. Singh,N.; Bhardwaj. S.A. Reviewing the role of coal bottom ash as an alternative of cement. *Constr. Build. Mater.* **2020**, *233*, 117276. https://doi.org/10.1016/j.conbuildmat.2019.117276
3. Feduik, R.S,; Smoliakov, A. K.; Timokhin, R. A.; Batarshin, V. O.; Yevdokimova, Yu. G. Using thermal power plants waste for building materials. IOP Publishing IOP Conf. Series: Earth and Environmental Science. **2017**, *87*, 092010. https://doi.org/10.1088/1755-1315/87/9/092010
4. Yu, J.; Lu, C.; Leung, C.K.Y.; Li, G. Mechanical properties of green structural concrete with ultrahigh-volume fly ash. *Constr. Build. Mater.* **2017**, *147*, 510–518. https://doi.org/10.1016/j.conbuildmat.2017.04.188.
5. Teixeira, E.R.; Mateus, R.; Camoes, A.F.; Bragança, L.; Branco, F.G. Comparative environmental life-cycle analysis of concretes using biomass and coal fly ashes as partial cement replacement material. *J. Clean. Prod.* **2016**, *112*, 4, 2221–2230. http://dx.doi.org/10.1016/j.jclepro.2015.09.124
6. ASTM C430-25. Standard Test Method for Fineness of Hydraulic Cement by the 45-μm (No. 325) Sieve. 2025, 3 p. https://clck.su/ogqcg
7. EN 197-1. Cement - Part 1: Composition, specifications and conformity criteria for common cements. 2000. 29 p. http://www.rucem.ru/yabbfiles/Attachments/EN-197-1.pdf?ysclid=mnr4zv8n5b285610497
8. GOST 31108-2020. Common cements. Specifications. Moscow, Standartinform. 2020. 20 p. https://www.status-grunt.ru/upload/bases/24.pdf?yclid=11130730052221140991
9. Durdziński, P.T.; Dunant, C.F.; Haha, M.B.; Scrivener, K.L. A new quantification method based on SEM-EDS to assess fly ash composition and study the reaction of its individual components in hydrating cement paste. *Cem. Concr. Res.* **2015**, *73*, 111–122. http://dx.doi.org/10.1016/j.cemconres.2015.02.008
10. Wu, R.D.; Dai, S.B.; Jian, S.W.; Huang, J.; Yang, L.; Li, B.D.; Nurmirzayev, A. Utilization of the circulating fluidized bed combustion ash in autoclaved aerated concrete: Effect of superplasticizer. *Constr. Build. Mater.* **2020**, *237*, 117644. https://doi.org/10.1016/j.conbuildmat.2019.117644
11. Zhang, N.; Yu, H.; Gong, W.; Liu, T.; Wang, N.; Tan, Yo.; Wu, C. Effects of low- and high-calcium fly ash on the water resistance of magnesium oxysulfate cement. *Constr. Build. Mater.* **2020**, *230*, 116951. https://doi.org/10.1016/j.conbuildmat.2019.116951
12. Deschner, F.; Winnefeld, F.; Lothenbach, B.; Seufert, S.; Schwesig, P.; Dittrich, S.; Goetz-Neunhoeffer, F.; Neubauer Ju.. Hydration of Portland cement with high replacement by siliceous fly ash. *Cem. Concr. Res.* **2012**, *42*, 1389-1400. https://doi.org/10.1016/j.cemconres.2012.06.009
13. Sharonova, O.M.; Solovyov, L.A.; Oreshrina, N.A.; Yumashev, V.V.; Anshits, A.G. Composition of high-calcium fly ash middlings selectively sampled from ash collection facility and prospect of their utilization as component of cementing materials. *Fuel Process. Technol.* **2010**, *91*, 6, 573-581. https://doi.org//10.1016/j.fuproc.2010.01.00
14. Ilic, M.; Cheeseman, C.; Sollars, C.; Knight, J. Mineralogy and mi-crostructure of sintered lignite coal fly ash. *Fuel.* **2003**, *82*, 331–336. https://doi.org//10.1016/S0016-2361(02)00272-7
15. Tishmack, J.K; Olek, J.; Diamond, S.; Sahu, S. Characterization of pore solutions expressed from high-calcium fly-ash-water pastes. *Fuel.* **2001**, *80*, 815–819. https://doi.org//10.1016/S0016-2361(00)00160-5
16. Escalante-Garcia, J.-I.; Sharp, J.H. The chemical composition and microstructure of hydration products in blended cements. *Cem. Concr. Compos.* **2004**, *26*, 967-976. https://doi.org//10.1016/j.cemconcomp.2004.02.036
17. Supit, S.V.M.; Shaikh, F.U.A.; Sarker, P.K. Effect of ultrafine fly ash on mechanical properties of high volume fly ash mortar. *Constr. Build. Mater.* **2014**, *51*, 278-286. http://dx.doi.org/10.1016/j.conbuildmat.2013.11.002

 doi:10.20944/preprints202604.1189.v1

18. Lothenbach, B.; Scrivener, K.; Hooton, R.D. Supplementary cementitious materials. *Cem. Concr. Res.* **2011**, *41*, 1244-1256. https://doi.org//10.1016/j.cemconres.2010.12.001
19. Aughenbaugh, K.L.; Chancey, R.T.; Stutzman, P.; Juenger, M.C.; Fowler, D.W. An examination of the reactivity of fly ash in cementitious pore solutions. *Mater. Struct.* **2013**, *46*, 869–880. https://doi.org//10.1617/s11527-012-9939-6
20. Pratiwi, W.D.; Triwulan; Ekaputri, J.J.; Fansuri, H. Combination of precipitated-calcium carbonate substitution and dilute-alkali fly ash treatment in a very high-volume fly ash cement paste. *Constr.Build. Mater.* **2020**, *234* , 117273. https://doi.org/10.1016/j.conbuildmat.2019.117273
21. Johnson, A.; Catalan, L.J.J.; Kinrade, S.D. Characterization and evaluation of fly-ash from co-combustion of lignite and wood pellets for use as cement admixture. *Fuel*. **2010**, *89*, 3042–3050. https://doi.org//10.1016/j.fuel.2010.05.027
22. Kutchko, B.G.; Kim, A.G. Fly ash characterization by SEM–EDS. *Fuel.* **2006**, *85*, 2537–2544. https://doi.org//10.1016/j.fuel.2006.05.016
23. Kim, T.; Davis, J.M.; Ley, M.T.; Kang, S.; Amrollahi. P. Fly ash particle characterization for predicting concrete compressive strength. *Constr. Build. Mater.* **2018**, *165*, 560–571. https://doi.org/10.1016/j.conbuildmat.2018.01.059
24. Kang, S.; Lloyd, Z.; Kim, T.; Ley M.T. Predicting the compressive strength of fly ash concrete with the Particle Model. *Cem. Concr. Res.* **2020**, *137*, 106218. https://doi.org/10.1016/j.cemconres.2020.106218
25. Sharonova, O.M.; Yumashev, V.V.; Solovyov, L.A.; Anshits, A.G. The fine high-calcium fly ash as the basis of composite cementing material. *Mag. Civ. Eng*. **2019**, 60-70. https://doi.org//10.18720/MCE.91.
26. GOST 5382-2019. Cements and materials for cement production. Chemical analysis methods. Moscow, Standartinform. 2019, 66 p. https://rosgosts.ru/file/gost/77/150/gost_5382-2019.pdf?ysclid=mnr4ur7shu915779500
27. Sharonova, O.M.; Solovyov, L.A.; Anshits, A.G. The influencing factors for the strength enhancement of composite materials made up of fine high-calcium fly ash. *Adv. Concrete Constr.* **2023**, *16*, 3, 169-176. https://doi.org/10.12989/acc.2023.16.3.169
28. Han, H. X.; Yang, J.; Feng, J.; Zhou, C.; Wang, X. Research on hydration mechanism of ultrafine fly ash and cement composite. *Constr. Build. Mater.* **2019**, *227*, 116697. https://doi.org/10.1016/j.conbuildmat.2019.116697